submitted to *Geophys. J. Int.*

# Structurally-constrained inversion by means of a Minimum Gradient Support regularizer: Examples of FD-EMI data inversion constrained by GPR reflection data

Tim Klose[1⋆], Julien Guillemoteau[1], Giulio Vignoli[2,3], Judith Walter[4], Andreas Herrmann[5], Jens Tronicke[1]

[1] *University of Potsdam, Institute of Geosciences, Karl-Liebknecht-Str. 24-25, 14476 Potsdam-Golm, Germany*

[2] *University of Cagliari, Department of Civil, Environmental Engineering and Architecture, 09123 Cagliari, Italy*

[3] *Geological Survey of Denmark and Greenland (GEUS), Department of Groundwater and Quaternary Geology Mapping, 8000 Aarhus, Denmark*

[4] *State Office for Mining, Geology and Natural Resources Brandenburg, Inselstr. 26, 03046 Cottbus, Germany*

[5] *Humboldt-Universtität zu Berlin, Thaer-Institute of Agricultural and Horticultural Sciences, Albrecht-Thaer-Weg 2, 14195 Berlin, Germany*

**SUMMARY**

Many geophysical inverse problems are known to be ill-posed and, thus, requiring some kind of regularization in order to provide a unique and stable solution. A possible approach to overcome the inversion ill-posedness consists in constraining the position of the model interfaces. For a grid-based parameterization, such a structurally-constrained inversion can be implemented by adopting the usual smooth regularization scheme in which the local weight of the regularization is reduced where an interface is expected. By doing so, sharp contrasts are promoted at interface locations while standard smoothness constraints keep affecting the other regions of the model. In this work, we present a structurally-constrained approach and test it on the inversion of frequency-domain elec-

tromagnetic induction (FD-EMI) data using a regularization approach based on the Minimum Gradient Support (MGS) stabilizer, which is capable to promote sharp transitions everywhere in the model, i.e., also in areas where no structural a priori information is available. Using 1D and 2D synthetic data examples, we compare the proposed approach to a structurally-constrained smooth inversion as well as to more standard (i.e., not structurally-constrained) smooth and sharp inversions. Our results demonstrate that the proposed approach helps in finding a better and more reliable reconstruction of the subsurface electrical conductivity distribution, including its structural characteristics. Furthermore, we demonstrate that it allows to promote sharp parameter variations in areas where no structural information are available. Lastly, we apply our structurally-constrained scheme to FD-EMI field data collected at a field site in Eastern Germany to image the thickness of peat deposits along two selected profiles. In this field example, we use collocated constant offset ground-penetrating radar (GPR) data to derive structural a priori information to constrain the inversion of the FD-EMI data. The results of this case study demonstrate the effectiveness and flexibility of the proposed approach.

**Key words:** Controlled source electromagnetics (CSEM) – Inverse theory – Electrical properties – Ground penetrating radar – Frequency Domain Electromagnetics – Inversion

## 1 INTRODUCTION

Frequency-domain electromagnetic induction (FD-EMI) data collected by loop-loop sensors are widely used to investigate near-surface electrical properties, in particular electrical conductivity $\sigma$. Typical fields of application include archeological prospection (De Smedt et al. 2014; Guillemoteau et al. 2019; Kristiansen et al. 2022), precision agriculture (Jadoon et al. 2015; Rudolph et al. 2016; Brogi et al. 2019; von Hebel et al. 2021), hydrological studies (Vereecken et al. 2015; von Hebel et al. 2014; Martini et al. 2017; Paepen et al. 2020), mapping subsurface utilities (Guillemoteau & Tronicke 2015; Thiesson et al. 2018; Couchman & Everett 2022), and exploring peat deposits (Altdorff et al. 2016; Guillemoteau et al. 2017; Beucher et al. 2020; Clément et al. 2020; McLachlan et al. 2020; Klose et al. 2022). Inversion of FD-EMI data is a typical example of a ill-posed problem, entailing the need

* tim.klose@uni-potsdam.de

of introducing a regularization term in the objective functional to be minimized in order to find the unique and stable solution compatible with the data and the prior information (formalized, indeed, via the regularizer). A standard approach to implement such a stabilization consists of applying spatial smoothness constraints (Constable et al. 1987); in this case, the unique solution selected by the algorithm is the one - still compatible with the data - that is characterized by the minimum spatial variation of the model parameters. However, often geologies consist of blocky structures and sharp interfaces rather than smoothly varying transitions, and, in these cases, the prior information enforced via traditional (smooth) regularizers would be in contradiction with the actual investigated targets. One possible regularization strategy to address this issue is based on the Minimum Gradient Support (MGS) stabilizer (Portniaguine & Zhdanov 1999; Zhdanov 2002), which allows retrieving sparse/sharp solutions. Such MGS regularization strategies have been proposed for the inversion of gravity data (Last & Kubik 1983), electrical resistivity tomography (ERT) data (Blaschek et al. 2008; Fiandaca et al. 2015; Thibaut et al. 2021), seismic dispersion curves (Vignoli et al. 2021; Guillemoteau et al. 2022), travel-time tomography (Zhdanov et al. 2006; Ajo-Franklin et al. 2007; Vignoli et al. 2012), and FD-EMI data (Deidda et al. 2020; Klose et al. 2022). In the MGS schemes, the level of sparsity can be easily tuned by means of the so-called focusing parameter. Basically, such a parameter defines the threshold for which a model parameter variation will be considered significant (Vignoli et al. 2021). Hence, ”small” values of the focusing parameter promote sharp solutions, whereas ”large” values allow the reconstruction of smooth spatial distributions of the investigated physical parameters (Vignoli et al. 2015, 2021). So far, no implementations of MGS have incorporated local choices of the focusing parameter: A unique value has been always chosen for the entire inversion domain. On the other hand, as will be discussed in the rest of the present research, there are situations where the capability of having values of the focusing parameter depending on the location might be advantageous.

FD-EMI data, similarly to other electrical and electromagnetic (EM) measurements (e.g., ERT data), are mainly sensitive to the bulk material properties (Constable & Weiss 2006). Also for this reason, these data typically show lower spatial resolution compared, for example, to ground-penetrating radar (GPR) and seismic reflection data, which are mainly sensitive to structure and parameter contrasts (Doetsch et al. 2012; Akca & Gölebatmaz 2021). Thus, in the literature different approaches have been proposed to incorporate additional structural information from GPR or seismic data into the inversion of electrical or EM data in order to improve the stability and the resolution capabilities of the final result (e.g., Wagner & Uhlemann 2021). A common implementation for incorporating structural a priori information in such structurally-constrained inversion approaches is to down-weight or completely remove the smoothness constraints around expected interfaces. For example, Brown et al. (2012) proposed a structurally-constrained inversion approach of controlled-source electromagnetic

data using regularization weights based on gradients of the seismic velocity model, and Yan et al. (2017) discussed a magnetotelluric inversion approach, where the weights of the regularizing smoothness constraints are based on the envelope attribute of reflection seismics. Subsurface structural information can also be interpreted and extracted from processed GPR or reflection seismic images by picking coherent reflection events. Assuming that the resulting horizons represent bounding surfaces (i.e., contrasts in physical parameters), they may be considered structural a priori information for constraining the inversion of electrical or EM data. For example, picked interfaces derived from GPR data have been used to constrain ERT data inversion (Doetsch et al. 2012) and magnetic resonance tomography (Jiang et al. 2020), whereas interfaces from seismic reflection data have been used to constrain ERT data inversion (Bergmann et al. 2014; Uhlemann et al. 2017) and magnetotelluric data inversion (Favetto et al. 2007). In all of these structurally-constrained inversion approaches, the capability to reconstruct a sharp interface relies merely on the structural a priori information as extracted from GPR or seismic reflection data. Clearly, in the standard (smooth) approaches, model areas where no structural information (concerning the presence of interfaces) is available can be reconstructed solely by enforcing smooth constraints (and producing, in turn, overall smooth solutions). Instead, in the present research, we present a structurally-constrained inversion approach for FD-EMI data based on the MGS regularization. While we exploit the beneficial characteristics of the MGS approach as an overall regularization scheme, we can make use of the additional structural prior information. By doing so, the inversion approach is able to promote potentially sharp model solutions also in areas where the structural prior information is not explicitly available. In this work, we intend to gain the structural a priori information from GPR data. In the following, we present in detail how the structural a priori information is integrated into the MGS regularization approach. Then, we use 1D and 2D synthetic examples, forward modeled with a full non-linear modeling approach, to show the principles of the proposed inversion approach and to evaluate its capabilities. Finally, we apply the proposed approach to a field data set acquired in Kremmen, Germany, to image peat deposits.

## 2 THEORY

We formulate the inversion of FD-EMI multi-configuration data as an optimization problem where we minimize the following objective function $\phi$ in an iterative fashion:

$$\phi = \sum_{i=1}^{N_d} \left[ (\boldsymbol{W}\boldsymbol{d}^{\boldsymbol{obs}})_i - (\boldsymbol{W}\boldsymbol{f}(\boldsymbol{m}))_i \right]^2 + \alpha\phi_m(\boldsymbol{m}). \quad (1)$$

Here, $N_d$ represents the total number of data points, $\boldsymbol{W}$ the data weighting matrix depending on data uncertainties, $\boldsymbol{d}^{\boldsymbol{obs}}$ the observed data vector, $\boldsymbol{f}(\boldsymbol{m})$ the forward modelling based on a full 1D

layered medium theory (see Wait 1982; Ward & Hohmann 1988), $\boldsymbol{m}$ the model parameter vector, $\alpha$ a Lagrangian parameter, and $\phi_m$ the stabilizer incorporating the constraints enforced on the model parameters. Similarly to Guillemoteau et al. (2016) and Klose et al. (2022), we convert the given low induction number (LIN) apparent conductivities $\sigma_a^{LIN}$ (McNeill 1980), typically supplied by FD-EMI multi-configuration sensors, into robust apparent conductivity $\sigma_a$ values and, then, define $\boldsymbol{d^{obs}}$ as

$$\boldsymbol{d^{obs}} = [log\sigma_{a,1}, log\sigma_{a,2}, \ldots, log\sigma_{a,N_d}]^T. \tag{2}$$

The vector $\boldsymbol{m}$ is defined as the logarithm of the electrical conductivity $\sigma$:

$$\boldsymbol{m} = [log\sigma_1, log\sigma_2, \ldots, log\sigma_{N_m}]^T, \tag{3}$$

where $N_m$ is the total number of model parameters. While inverting a single sounding, $N_d$ represents the number of configurations and $N_m$ the number of layers of the 1D model. When performing a 1D laterally constrained inversion (LCI) of a number of soundings to reconstruct a (pseudo-)2D model, $N_d$ is the total number of data points (i.e., the number of configurations multiplied by the number of adjacent soundings considered in the LCI), and $N_m$ is the number of cells discretizing the 2D model.

The goal of the present study is to incorporate structural constraints as derived from GPR data into the formulated inverse problem. For such a grid-based inversion procedure, a common approach is to implement a smooth inversion, in which the weight of the smoothness constraints is decreased for model areas where a sharp interface is expected (e.g., Brown et al. 2012; Doetsch et al. 2012; Yan et al. 2017; Wagner & Uhlemann 2021). For such a structurally-constrained smooth inversion approach (C-S), the model regularization function can be defined as

$$\phi_m^{C-S}(\boldsymbol{m}) = \sum_{j=1}^{N_m} \frac{(\boldsymbol{Dm})_j^2}{\boldsymbol{v}_j^2 + \beta^2}, \tag{4}$$

where $\boldsymbol{D}$ is a gradient operator, $\boldsymbol{v}$ contains the (spatially varying) weights of the smooth constraints at the numerator (with higher values in areas where abrupt changes are expected), and $\beta$ defines a threshold from which the weights in $\boldsymbol{v}$ are considered significant and prevents singularities.

The non-linear MGS regularization (Portniaguine & Zhdanov 1999) is defined at iteration $s$ as:

$$\phi_m^{MGS}(\boldsymbol{m}_s) = \sum_{j=1}^{N_m} \frac{(\boldsymbol{Dm}_s)_j^2}{(\boldsymbol{Dm}_{s-1})_j^2 + \epsilon^2}, \tag{5}$$

where $\epsilon$ is the focusing parameter controlling the sharpness/sparsity of the solution (Vignoli et al. 2015, 2021). As pointed out in Guillemoteau et al. (2022), the analogy between Eq. 4 and Eq. 5 shows that the MGS constraints can be seen as structural constraints, which are defined by the gradient of $\boldsymbol{m}$ of the preceding iteration. This process yields a non-linear iterative focusing/sharpening of the model.

Similar conclusions can be drawn, from a Bayesian perspective, as discussed in depth, for example, in Vignoli et al. (2021).

In order to ensure sharp models while applying structural constraints (structurally-constrained MGS inversion, C-MGS), we propose to extend Eq. 5 as follows:

$$\phi_m^{C-MGS}(\boldsymbol{m}_s) = \sum_{j=1}^{N_m} \frac{(\boldsymbol{D}\boldsymbol{m}_s)_j^2}{(\boldsymbol{D}\boldsymbol{m}_{s-1})_j^2 + (\epsilon \cdot [1 + \boldsymbol{g}])_j^2}, \tag{6}$$

where $\boldsymbol{g}$ describes the structural constraints and is characterized by values greater than zero in model regions where interfaces are expected. Compared to Eq. 4, Eq. 6 is based on two different sources of information: (i) the available structural a priori information and (ii) the structural constraints derived from the model of the preceding iteration (or starting model $\boldsymbol{m}_0$ at iteration $s$ = 1). This allows for model sharpening in all areas of the model (except where $\epsilon \gg \boldsymbol{D}\boldsymbol{m}_{s-1}$) even in areas where no a priori information concerning the presence of sharp transitions is available. This is a desired characteristic because in practice prior structural information and assumptions are often not available for the entire model domain.

Using Eq. 6 with a pseudo-2D LCI inversion strategy results in

$$\phi_m^{C-MGS}(\boldsymbol{m}_s) = \sum_{j=1}^{N_m} \left[ \frac{(\boldsymbol{D_z}\boldsymbol{m}_s)_j^2}{(\boldsymbol{D_z}\boldsymbol{m}_{s-1})_j^2 + (\epsilon \cdot [1 + \boldsymbol{g_z}])_j^2} + w \frac{(\boldsymbol{D_x}\boldsymbol{m}_s)_j^2}{(\boldsymbol{D_x}\boldsymbol{m}_{s-1})_j^2 + (\epsilon \cdot [1 + \boldsymbol{g_x}])_j^2} \right], \tag{7}$$

where $\boldsymbol{D_z}$ and $\boldsymbol{D_x}$ are first-order spatial differential operators for the model $\boldsymbol{m}$ in the vertical $z$- and lateral $x$-direction, respectively, $w$ describes the relative weight of the lateral constraints, and $\boldsymbol{g_z}$ and $\boldsymbol{g_x}$ contain the available structural a priori information for the vertical $z$- and lateral $x$-direction, respectively. In the $\boldsymbol{g}$ vectors, a value equal to zero indicates that no interface is expected near the corresponding model cell along the respective direction. In contrast, a value greater than zero indicates an interface. The maximum values in $\boldsymbol{g_z}$ and $\boldsymbol{g_x}$ and the width of a structural feature around an expected interface (i.e., $\boldsymbol{g_z}$ and $\boldsymbol{g_x}$ values $> 0$) can be used, for example, to reflect the accuracy and reliability of the available a priori structural information.

In order to minimize the objective function $\phi$ (as defined in Eq. 1), we use an iterative procedure where $\boldsymbol{m}$ at the iteration $s$ is calculated by (Constable et al. 1987; Aster et al. 2005):

$$\boldsymbol{m}_s = [\boldsymbol{J}^T(\boldsymbol{m}_{s-1})\boldsymbol{C_d}\boldsymbol{J}(\boldsymbol{m}_{s-1}) + \alpha_s \boldsymbol{S}(\boldsymbol{m}_{s-1})]^{-1} \boldsymbol{J}^T(\boldsymbol{m}_{s-1})\boldsymbol{C_d}[\boldsymbol{d^{obs}} - \boldsymbol{f}(\boldsymbol{m}_{s-1}) + \boldsymbol{J}(\boldsymbol{m}_{s-1})\boldsymbol{m}_{s-1}]. \tag{8}$$

Here, $\boldsymbol{J}$ is the Jacobian of the forward problem, $\boldsymbol{C_d} = \boldsymbol{W}^T\boldsymbol{W}$ is the approximation of the data covariance matrix, $\boldsymbol{m}_s$ is the model parameter vector of the preceding iteration (at iteration $s$ = 1, we use a starting model $\boldsymbol{m}_0 = log(\bar{\boldsymbol{\sigma}}_{\boldsymbol{a}})$), and $\boldsymbol{S}$ is the regularization matrix defined as

$$\boldsymbol{S} = \boldsymbol{L_z}^T\boldsymbol{L_z} + w\boldsymbol{L_x}^T\boldsymbol{L_x}, \tag{9}$$

with $\boldsymbol{L_z}$ and $\boldsymbol{L_x}$ (for the proposed C-MGS approach) being

$$\boldsymbol{L_z^{C-MGS}} = \frac{\boldsymbol{D_z}}{\sqrt{(\boldsymbol{D_z m}_{s-1})^2 + (\epsilon \cdot [1 + \boldsymbol{g_z}])^2}} \quad \text{and} \quad \boldsymbol{L_x^{C-MGS}} = \frac{\boldsymbol{D_x}}{\sqrt{(\boldsymbol{D_x m}_{s-1})^2 + (\epsilon \cdot [1 + \boldsymbol{g_x}])^2}}. \tag{10}$$

Here, it is important to note that $\boldsymbol{S}$ depends on $\boldsymbol{m}_{s-1}$. In order to facilitate the $\alpha$ search at each iteration by keeping it in the same range, we follow Guillemoteau et al. (2022) and Klose et al. (2022) by normalizing $\boldsymbol{S}$ as follows:

$$\boldsymbol{S} = \frac{1}{\sum diag(\boldsymbol{L_z^T L_z})} \cdot [\boldsymbol{L_z^T L_z} + w \boldsymbol{L_x^T L_x}]. \tag{11}$$

For sake of completeness, and since it will be used later, for the C-S approach, $\boldsymbol{L_z}$ and $\boldsymbol{L_x}$ can be expressed as:

$$\boldsymbol{L_z^{C-S}} = \frac{\boldsymbol{D_z}}{\sqrt{\boldsymbol{v_z^2} + \beta^2}} \quad \text{and} \quad \boldsymbol{L_x^{C-S}} = \frac{\boldsymbol{D_x}}{\sqrt{\boldsymbol{v_x^2} + \beta^2}}, \tag{12}$$

where $\boldsymbol{v_z}$ and $\boldsymbol{v_x}$ contain the available structural a priori information for the vertical $z$- and lateral $x$-direction, respectively.

## 3 SYNTHETIC DATA EXAMPLES

In the following, we use a 1D synthetic example to investigate the basic applicability of the proposed C-MGS approach (Eqs. 7 - 11) including the sharpening effect, in particular, in areas where no prior structural information is available. Furthermore, in order to demonstrate the principles of our inversion approach for a more realistic 2D data set, we use the 2D synthetic example discussed in Klose et al. (2022). Both synthetic data sets simulate the data of a FD-EMI sensor placed at 0.25 m above ground, operating at a fixed frequency of 9 KHz and consisting of two horizontal coplanar (HCP) and two perpendicular (PERPx) configurations with coil spacings of 1 m, 2 m, 1.1 m, and 2.1 m, respectively. The simulated FD-EMI sensor, as well as the input subsurface models used for the synthetic examples, are chosen to be representative of the field data presented later, which were collected on a rather conductive peat layer covering a resistive sandy background.

### 3.1 1D synthetic data example

The 1D synthetic data set consists of a single sounding, where the input model is a three-layer case (black dashed line in Fig. 1). In this model, the first layer is 0.35 m thick with $\sigma_1$ = 0.04 S/m, the second layer is 1.45 m thick with $\sigma_2$ = 0.075 S/m, while the third layer (halfspace) is characterized by $\sigma_3$ = 0.007 S/m. We want to compare the vertically-constrained inversion (VCI; i.e., the inversion in which each sounding is handled individually and, consistently, the regularization acts uniquely in the vertical direction) results when using each of the two regularizers $\phi_m^{C-S}(\boldsymbol{m})$ and $\phi_m^{C-MGS}(\boldsymbol{m})$ (Eqs.

4 and 6, respectively), in particular in view of reconstructing an interface which is not described by any prior structural information. For this, only the deepest interface is assumed to be known. This can, for example, mimic the case in which the deeper interface is retrieved from collocated GPR traces. The first, shallower interface however is assumed to be unknown since, for example, the corresponding GPR reflection interferes with the direct ground wave and, thus, cannot be properly inferred. For the C-MGS approach, $\epsilon$ is set to a low value of 0.01 to ensure the sharpening effect. The number of layers in the model is set to 50, where the thickness of each layer increases towards deeper layers up to a maximum depth of around 4 m. Thus, in this, but also in all the other examples in the paper, the model discretization consists of layers characterized by fixed thicknesses ranging from 0.015 m to 0.15 m (at the maximum depth). In Fig. 1a, we show the VCI results for the two regularization approaches. As a reference, we also show two VCI results in which no prior assumptions are included, they are: (i) The smooth (Sm) regularized inversion (also known as Occam's regularizer) consisting of the C-S stabilizer in Eq. 4 in which $\boldsymbol{v}$ is actually a nonzero scalar (so with no dependency on the depth); and (ii) the standard MGS regularization (Eq. 5). Also in the standard MGS case, the value of the focusing parameter $\epsilon$ is equal to 0.01. As expected, the structurally-constrained inversions C-S and C-MGS outperform the associated (non-informed) unconstrained results Sm and MGS in reconstructing the deepest interface (at 1.9 m). It is worth noticing that, on the other hand, C-MGS provides better results of the deepest resistivity change also with respect to its smooth counterpart (the C-S). In fact, the C-S, like all smooth regularization schemes, in order to provide smoothly varying profiles, tends to overshoot the conductivity values above the interface and generate more gentle (and, in this case, wrong) variations around a depth of 1.9 m. This is clearly consistent with the additional requirements imposed respectively by the C-S and C-MGS regularizers: The model to be retrieved is characterized by sharp transitions that are inherently more consistent with the model sparsity promoted by the C-MGS algorithm.

When analyzing the area around the shallowest interface in more detail (Fig. 1b), we notice similar results for the C-MGS and MGS on one hand, and for the C-S and Sm inversions on the other. This is due to the fact that, for areas where no prior structural assumptions are set (shallower parts), the regularization matrix $\boldsymbol{S}$ for the C-MGS approach (Eqs. 10 and 11) remains pretty much the same compared to the inversion without any structural constraints. Differences in $\boldsymbol{S}$ for the C-MGS and MGS approaches are related to $\boldsymbol{m}$ of the preceding iteration which is different due to the overall prior assumptions. Analogously, for the C-S and Sm approach, $\boldsymbol{S}$ (Eqs. 11 and 12 for the C-S approach) remains the same for areas where no structural a priori information is defined. So, in short, for areas with no prior structural assumptions, the C-S approach promotes smooth results, while the C-MGS approach (using a small $\epsilon$ value) favors sharp solutions. Thus, the C-S inversion shows a high level of

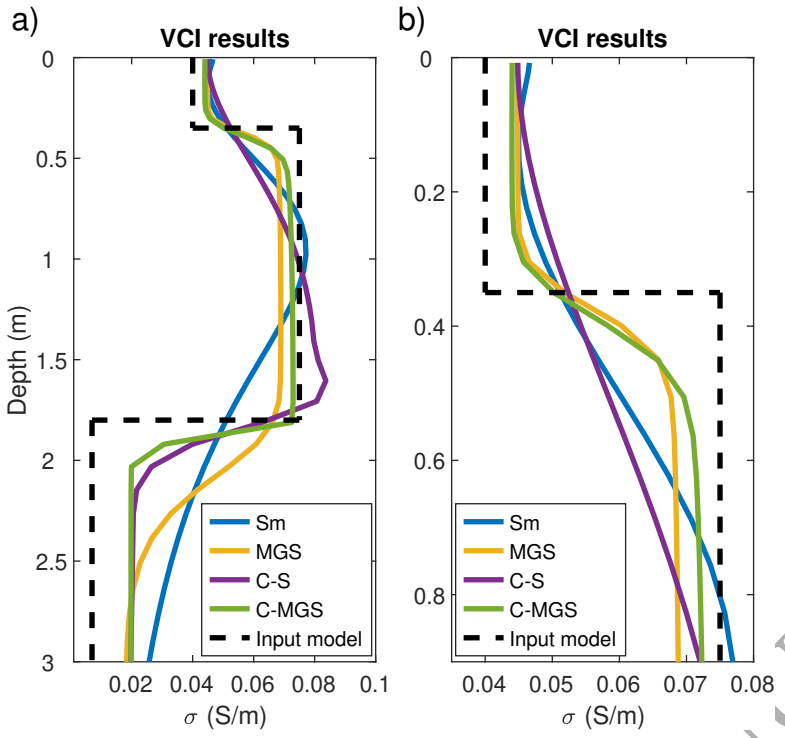


**Figure 1.** (a) VCI results for the 1D synthetic data example when using the Sm approach (blue), the MGS approach (yellow), the C-S approach (purple), and the C-MGS approach (green) in comparison to the input model (black dashed line) used to forward model the synthetic data set. (b) Zoom-in of (a) in order to analyze the differences around the shallowest interface between all VCI results in more detail.

smoothness in the shallow parts of the test model (i.e., at depths $< 0.8$ m) and, consequently, these model areas cannot be interpreted effectively in terms of interfaces. In comparison, when using the C-MGS approach, we notice a higher level of sharpness also around the shallowest blocky transition. These results demonstrates the capability of the C-MGS approach to provide a sharp solution also in model areas where no prior structural information is available. Overall, this preliminary test demonstrates that if sharp interfaces are expected, MGS-like regularizations consistently provide results that are more in agreement with the real targets. Moreover, if a priori information concerning the presence of a sharp conductivity variation is available, its inclusion in the inversion process clearly improves the quality of the reconstruction.

The differences in the inversion results of the C-S and the C-MGS approaches (Fig. 1) can be explained by the regularization matrix $\boldsymbol{S}$, which is updated in each iteration of the C-MGS inversion process considering the model $\boldsymbol{m}$ of the preceding iteration (Eqs. 10 and 11). In contrast, when using the C-S approach, $\boldsymbol{S}$ is not changing during the iterations (Eqs. 11 and 12). In Fig. 2, we show the diagonal values $\boldsymbol{S}_{ii}$ (corresponding to layers in the model with increasing depth) for each iteration for the VCI results shown in Fig. 1 when using the C-MGS approach (Fig. 2a) and the C-S approach (Fig.

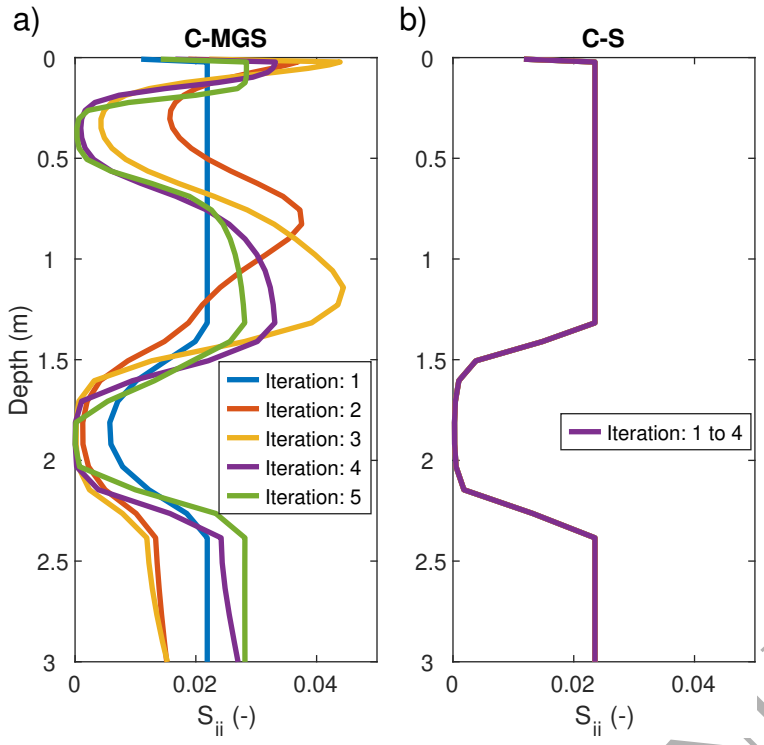


**Figure 2.** $\boldsymbol{S}_{ii}$ for each iteration of the inversion of the 1D synthetic data example shown in Fig. 1 when using (a) the C-MGS approach (and $\epsilon = 0.01$), and (b) the C-S approach.

2b). The $\boldsymbol{S}_{ii}$ values do not change iteration-by-iteration when using the C-S approach which leads to an overall smooth inversion result with a high level of (local) sharpness only in areas where the structural prior assumption enforces it. In contrast, when using the C-MGS approach, the $\boldsymbol{S}_{ii}$ values vary during the iterative process, which ensures a high level of sharpness in all areas of the model.

### 3.2 2D synthetic data example

The 2D synthetic data set has been simulated with a 3D non-linear forward modeling method based on the finite volume approach (Haber 2014). We use the input subsurface model studied in Klose et al. (2022), which consists of two layers with an interface depth varying between 0.3 m and 1.5 m along the profile (Fig. 3a). The electrical conductivities of the two homogeneous layers are 0.1 S/m for the upper layer and 0.01 S/m for the deepest one. The synthetic data set consists of 57 soundings with the soundings spaced 0.6 m. Besides, we add uncorrelated noise of $\pm 1$ mS/m to the original synthetic $\sigma_a^{LIN}$ measurements. Similar to the 1D synthetic example, we set the number of layers of the model equal to 50 with a thickness increasing with depth, down to around 4 m.

First, we perform a LCI following the MGS approach (Eq. 5) using $\epsilon = 0.01$ and $w = 0.5$ (without incorporating any prior structural information). The result is shown in Fig. 3b. Overall, the inversion

result is in good agreement with the input subsurface model indicating that the MGS approach is able to find effective solutions even when structural prior information is not available and explicitly incorporated into the inversion. Clearly, making use of this additional piece of information (the location of the sharp interface) can only enhance the reliability and resolution of the final result; in this respect, Fig. 3c shows the C-MGS model obtained by using the same settings of the previous (unconstrained) MGS inversion (i.e., $\epsilon$ = 0.01 and $w$ = 0.5). The used structural a priori information is described with the vectors $\boldsymbol{g_z}$ and $\boldsymbol{g_x}$ which are visualized in Figs. 3d-e. The vectors $\boldsymbol{g_z}$ and $\boldsymbol{g_x}$ are equal to zero except for model cells crossed by the interface which is assumed to be known in this example. Being the $z$- and $x$- components of the gradient of the structural prior model, $\boldsymbol{g_z}$ and $\boldsymbol{g_x}$ have nonzero values only near the interface, where they are proportional to the corresponding projection along the axes of the discretization grid. In this way, the values of $\boldsymbol{g_z}$ and $\boldsymbol{g_x}$ are properly balanced according to the local slope of the prior interface. Since the derivative calculation is prone to increase the effects of the possible roughness of the surfaces used as prior structural information, and as it is usually done, for example, in image processing before applying edge detecting filters (e.g., Feng et al. 2017), we apply a 2D-Gaussian filter to $\boldsymbol{g_z}$ and $\boldsymbol{g_x}$. In accordance with the physics of the used methodologies, the $z$-width of the filter is made increasing with depth. This strategy accounts for uncertainties in the available structural a priori information, in particular in the vertical direction. For example when the structural a priori information is extracted from collocated GPR data, the standard deviation of the applied Gaussian filter can be set proportionally to the standard deviation of the derived interface location/depth. Finally, both $\boldsymbol{g_z}$ and $\boldsymbol{g_x}$ are scaled to range from zero to a user-specified maximum value, where a value of zero indicates that no interface is expected. The higher the maximum value, the more the inversion approach is forced to promote an interface at the corresponding location in the model space. However, a higher maximum value also suppress the influence of the model $\boldsymbol{m}$ of the preceding iteration when computing $\boldsymbol{S}$ (Eqs. 10 and 11). Via numerical tests, a maximum value of $\boldsymbol{g_z}$ and $\boldsymbol{g_x}$ equal one has proven to be effective in assuring a good balance between the structural a priori information and the constraints derived from $\boldsymbol{m}$ of the preceding iteration. Klose et al. (2022) and Guillemoteau et al. (2022) have discussed the benefit of defining the model with the logarithm of $\sigma$ for making the choice of $\epsilon$ independent of the geological context. Here, it is important to note that this modeling strategy has a similar effect for the choice of $\boldsymbol{g_z}$ and $\boldsymbol{g_x}$ amplitudes. Indeed, in the log-space, the model gradients $\boldsymbol{Dm}_{s-1}$ in Eqs. 7 and 10 correspond to relative differences of $\sigma$, so similar tuning parameters for $\boldsymbol{g_z}$ and $\boldsymbol{g_x}$ work well even for significantly different geological contexts. In Fig. 3c, we show the inversion result of the C-MGS approach. When comparing it to the MGS approach (Fig. 3b), we clearly see that adding the available structural information leads to a better reconstruction of the input subsurface model. This includes not only a more precise reconstruction of the location of

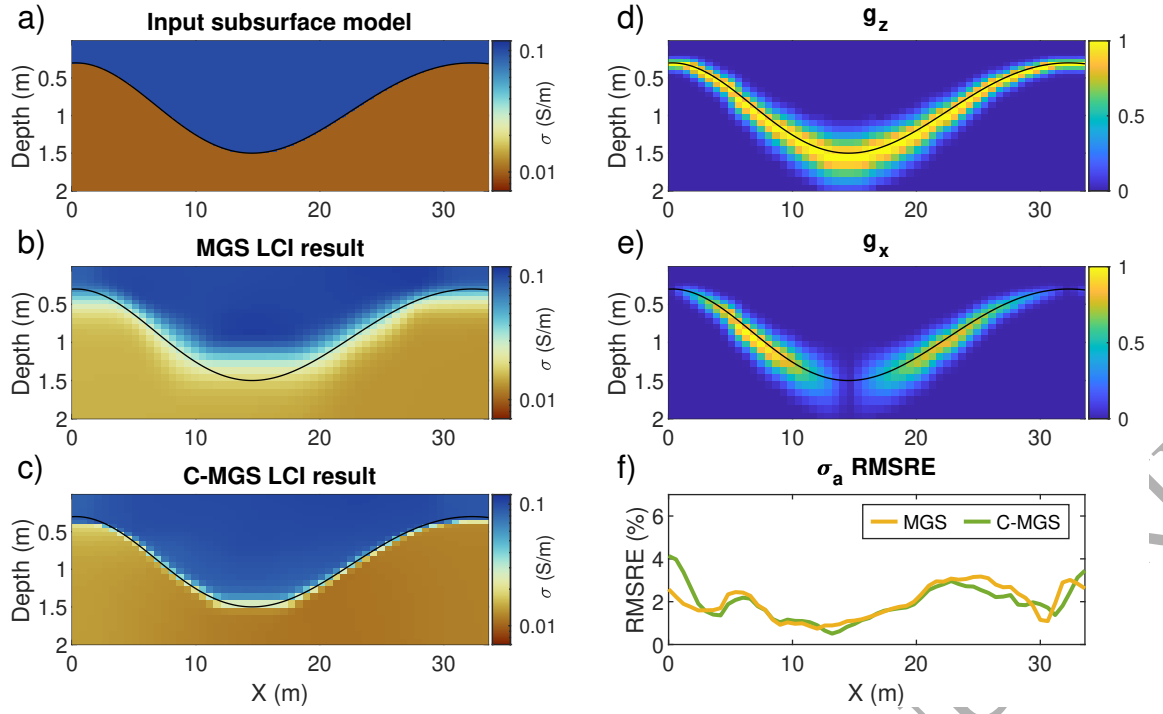


**Figure 3.** (a) Input subsurface model used to compute the 2D synthetic data example. (b) LCI result using the MGS approach with $\epsilon$ = 0.01 and $w$ = 0.5. (c) LCI result using the C-MGS approach with $\epsilon$ = 0.01 and $w$ = 0.5 and using (d) $\boldsymbol{g_z}$ and (e) $\boldsymbol{g_x}$ as structural a priori information. In (a) to (e), the black line indicates the true location of the interface. (f) $\sigma_a$ RMSRE misfit for the two shown LCI results.

the interface but also a more precise retrieval of the actual $\sigma$ values, especially, for the deepest, more resistive layer.

In Fig. 3f, we show the $\sigma_a$ root mean square relative error (RMSRE) along the entire profile for the two shown inversion results. Fig. 3f demonstrates quantitatively that each sounding is equally well inverted in terms of data fitting by both the MGS and the C-MGS algorithms. The same is true when we compare the overall data misfit for the entire section: The global RMSRE values for the MGS and the C-MGS schemes are indeed 2.10% and 2.09%, respectively. This demonstrates that adding the structural information into the inversion via the C-MGS strategy contributes to the selection of a unique and stable solution that adheres more to the expectations without impairing the data misfit.

## 4 FIELD DATA EXAMPLE

We now verify the applicability of the C-MGS approach on a field data example. We acquired our data set near Kremmen, Germany, to investigate peat deposits embedded in an overall sandy environment typical for a glacial environment. The peat is expected to show higher conductivities generally caused by high porosity, high pore fluid conductivity and high amount of organic material which is character-

ized by high surface conductivity. In comparison, lower conductivities of the sand correspond to lower porosity and the absence of organic material. To collect our FD-EMI data set, we used the DUALEM-21S (Dualem Inc.) system, which operates at a fixed frequency of 9 kHz. In this device, four different coil configurations are installed: two horizontal coplanar (HCP) and two perpendicular (PERPx) configurations with coil spacings of 1 m, 2 m, 1.1 m, and 2.1 m, respectively. During the survey, the device has been mounted on a cart at a height of 0.25 m above ground and the positions of the soundings have been recorded by using a self-tracking total station (Böniger & Tronicke 2010). In this study, we focus on two selected profiles (referred to as Profile 1 and Profile 2) with a total length of about 130 m each and an inline sounding spacing of about 0.5 m. Both profiles are parallel to each other, 15 m apart. Along these profiles, we performed a total of 14 push soundings to estimate the peat thickness. These ground-truth data were conducted by manually pushing a metal rod into the ground until no further penetration was possible. The structural information to be incorporated into the proposed C-MGS approach is extracted from GPR data collected along the same profiles. The GPR data have been acquired with a constant offset of 0.75 m, using a pair of 100 MHz antennas, mounted on a sledge, and whose locations have been monitored - similarly to the corresponding FD-EMI measurements - via a self-tracking station.

As a reference and in a similar fashion as in Klose et al. (2022), we first perform several LCI runs using the MGS approach (Eq. 5) with three different values for $\epsilon$ to invert the FD-EMI data collected along Profile 1 (Figs. 4a-c) and Profile 2 (Figs. 4d-f). Also in this case, for the inversion, the model consists of 50 layers of thicknesses increasing with depth and the bottom layer at around 4 m. The LCI results of the two profiles in Fig. 4 can be considered equivalent in terms of data misfit as their RMSRE values are comparable: between 1.01% and 1.06% for Profile 1, and between 1.08% to 1.12% for Profile 2. In general, all results show the same main features: (i) a shallow conductive body ($\sigma >$ 0.04 S/m), which can be interpreted as the peat layer; (ii) the peat conductivity increasing along the profile; (iii) below the peat, a lower conductivity unit ($\sigma <$ 0.02 S/m) associated with a sand layer; (iv) for both profiles, the peat thickness reaches its maximum (around 1.5 m) between X = 55 m and X = 90 m; (v) near the surface, less conductive anomalies, from X = 20 m to X = 55 m, for Profile 1 and, from X = 20 m to X = 80 m, for Profile 2. Clearly, even if all solutions are equally compatible with the data, the more sparse results ($\epsilon$ = 0.01) allow inferring the varying thickness of the peat more precisely. Having noticed this, the next step is to check the improvement brought by the structural information deducted from data of different origins (i.e., the locations of the GPR horizons).

The GPR data have been processed using a standard processing sequence, including direct-current (DC) shift removal, zero-time correction, bandpass filter to suppress low- and high-frequency noise, and a singular value decomposition (SVD) based filter (e.g., Cagnoli & Ulrych 2001) to suppress the

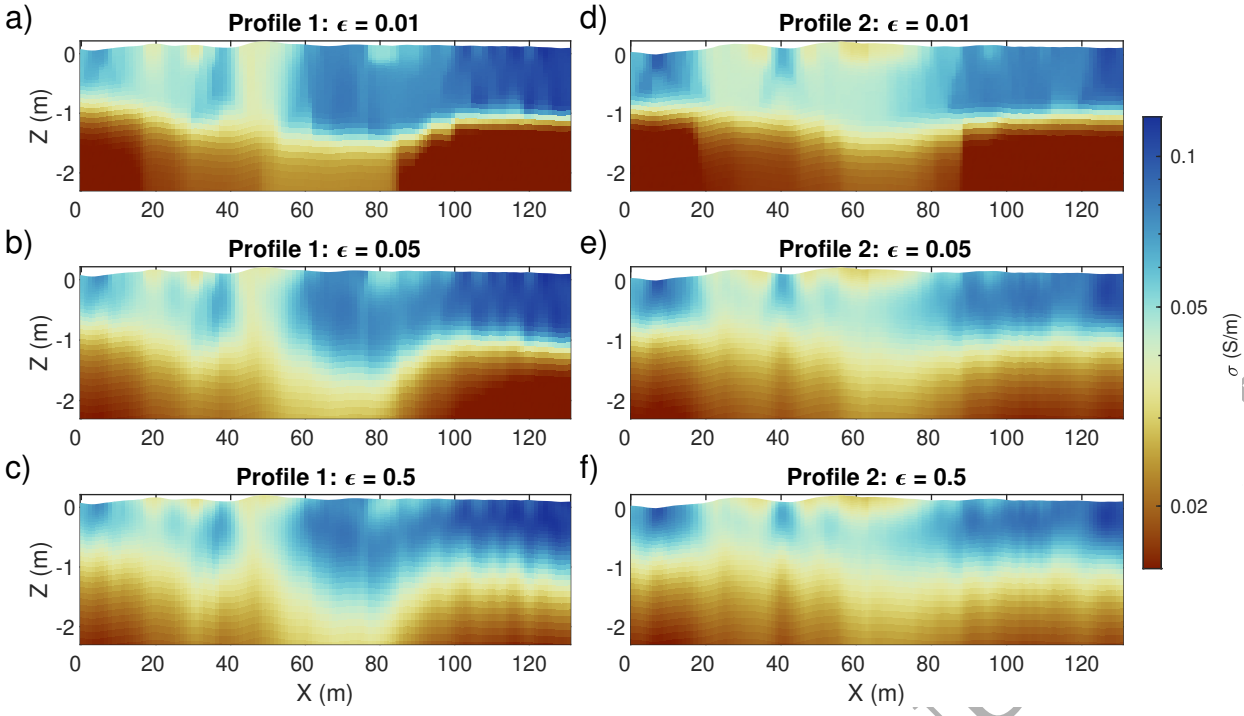


**Figure 4.** LCI results using the MGS approach for Profile 1 using (a) $\epsilon$ = 0.01 and $w$ = 0.5, (b) $\epsilon$ = 0.05 and $w$ = 0.5, and (c) $\epsilon$ = 0.5 and $w$ = 0.5. LCI results using the MGS approach for Profile 2 using (d) $\epsilon$ = 0.01 and $w$ = 0.5, (e) $\epsilon$ = 0.05 and $w$ = 0.5, and (f) $\epsilon$ = 0.5 and $w$ = 0.5. All shown LCI results can be seen as equivalent solutions in terms of data misfit.

arrivals of the direct waves (i.e., air and ground wave). Afterwards, the data have been interpolated to a regular trace spacing of 0.2 m using a 2D gridding approach. We also estimated the velocity of the peat deposit from additional common mid-point (CMP) data sets. Using spectral velocity analysis we derived a peat velocity of about 0.034 m/ns, which we use for the final Kirchhoff migration and time-to-depth conversion of the two common-offset GPR profiles. The resulting processed GPR Profiles 1 and 2 are shown in Figs. 5a and d, respectively. In both profiles, we see one major undulating reflector which is in good agreement with the base of the peat deposits as inferred from the push soundings (black vertical lines). Therefore, we interpret this reflector as associated to the peat-sand interface. Although some discrepancies in depth (in the order of 0.1 m to 0.2 m) are visible, the overall agreement between the GPR and push sounding data confirms our interpretation including the peat velocity as derived from CMP data and also indicates that there are no critical lateral subsurface variations in GPR velocity along the two profiles.

For GPR Profile 1 and 2, the main reflector has been picked manually (red dashed line in Figs. 5a and d) considering both the information from the processed GPR data and the push sounding data. In Profile 1, the reflector is lost in the GPR data around 50 m $\lesssim$ X $\lesssim$ 80 m and X $\gtrsim$ 110 m. In general,

we observe lower amplitudes of the reflected signal at X $\gtrsim$ 50 m indicating higher signal attenuation related, for example, to increased $\sigma$ values. In Profile 2, the reflector is lost at the end of the profile (X $\gtrsim$ 120 m) and the amplitudes of the reflected signal decrease at X $\gtrsim$ 80 m. These observations are in good agreement with the inversion results shown in Fig. 4; i.e., in areas with increased $\sigma$ values within the peat body, the attenuation increases and, thus, the amplitude of the reflected GPR signal decreases. Furthermore, for Profile 1, the reflector is lost where the FD-EMI results indicate maximum peat thickness (i.e., 55 m $\lesssim$ X $\lesssim$ 90 m). In summary, losing the main reflector can therefore be explained by either increased values in peat thickness or increased values in peat electrical conductivity.

The structural information gained from the GPR data and the push soundings is translated into $\boldsymbol{g_z}$ and $\boldsymbol{g_x}$ (Eq. 7) in the same fashion as previously explained for the 2D synthetic data case (see Figs. 5b-c and 5e-f). For areas where no peat-sand interface information is available, the derived peat-sand interface is interpolated or extrapolated. For those areas, the width of the Gaussian filter applied to $\boldsymbol{g_z}$ and $\boldsymbol{g_x}$ is increased to account for increased uncertainty in the structural a priori information. In Eq. 10, we see that even for areas where $\boldsymbol{g_z} = 0$ and $\boldsymbol{g_x} = 0$, $\boldsymbol{L_z^{C-MGS}}$ and $\boldsymbol{L_x^{C-MGS}}$ can change at each iteration due to the updates of the model $\boldsymbol{m}_{s-1}$. Thus, where no structural information is available (and, so, $\boldsymbol{g_z}$ and/or $\boldsymbol{g_x}$ are zero), the C-MGS returns to behave as the standard sparse regularization MGS. However, since the peat thickness is not expected to change rapidly over the profile, it was reasonable to enforce some lateral continuity to the peat-sand interface and, consistently, proceed with a mere interpolation/extrapolation of the horizon location where signs of the interface were missing.

Fig. 6 shows, for Profile 1 and Profile 2, the best (in terms of the reconstruction quality of the assumed peat-sand interface) LCI results when using the MGS (Figs. 6a and e) and the C-MGS approach (Figs. 6b and f) together with the obtained peat thickness from our push sounding data (black lines) and the derived peat-sand interface (red dashed line). All inversion parameters are the same for each of the shown results (i.e., $\epsilon$ = 0.01 and $w$ = 0.5). The only difference is that, for the C-MGS approach, $\boldsymbol{g_z}$ and $\boldsymbol{g_x}$ (Figs. 5b-c and e-f) have been considered during the inversion process. Incorporating this additional information leads to a more precise and neat reconstruction of the peat-sand interface and a more homogeneous reconstruction of $\sigma$ within the sandy substratum. In terms of global and local data misfit the MGS and C-MGS inversion results can be considered to be equivalent (Figs. 6d and h). In Figs. 6c and g, the calculated and observed robust apparent conductivities are compared. Thus, it is evident from all panels in Fig. 6 that, by incorporating in the C-MGS scheme the additional structural information about the location of the interface, the retrieved solution is, at the same time: (i) equally compatible with the observation, and (ii) in very good agreement with the geological information originated via other methodologies (geophysical and not). Thereby, the trustworthiness of the structural interpretation is not only justified by our GPR data but also by the ability to fit the

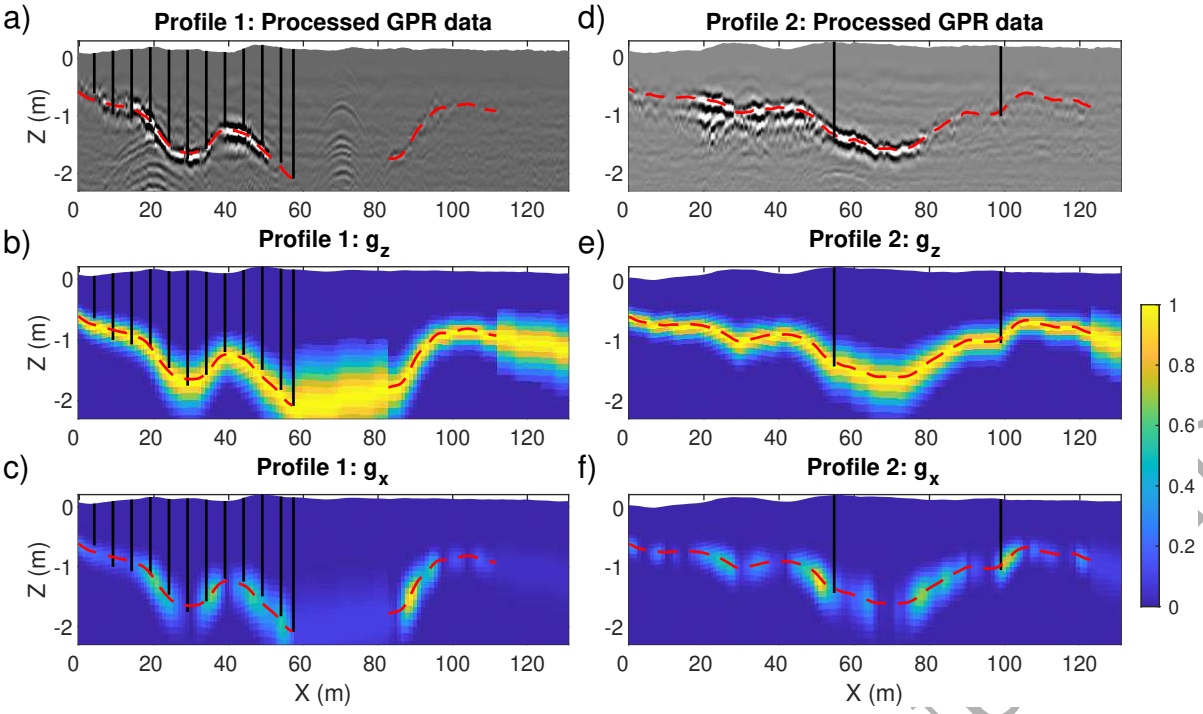


**Figure 5.** (a) Processed GPR data along Profile 1 and the structural prior information derived from (a) in terms of (b) $g_z$ and (c) $g_x$. (d) Processed GPR data along Profile 2 and the structural prior information derived from (d) in terms of (e) $g_z$ and (f) $g_x$. In (a) to (f), the black vertical lines indicate the peat thickness as derived from push sounding data, and the red dashed lines indicate the peat-sand interface interpreted from GPR and push sounding data.

FD-EMI data equally well when incorporating the available structural information. Thus, the resulting C-MGS results can be used for a more reliable interpretation of subsurface structures (here, focus on peat thickness) and of the lateral variability of $\sigma$ within the peat body.

Similar to Fig. 1, we compare in Fig. 7 the 1D results of different LCI approaches; i.e., the Sm, MGS, C-S, and C-MGS results at X = 78.7 m along Profile 1. At this selected position, the peat-sand interface is located at around 2 m depth as deduced by the GPR data. The Sm approach results in a smooth model where the peat-sand transition is blurred whereas, in the MGS reconstruction, the same interface is located at a shallower depth with respect to its presumable position. In the shallow portions of the retrieved conductivity profiles (see zoom-in in Fig. 7b), a superficial anomaly, down to 0.3 m, can be deduced almost identically in both MGS and C-MGS results; this anomaly can be interpreted as caused by different levels of peat decomposition.

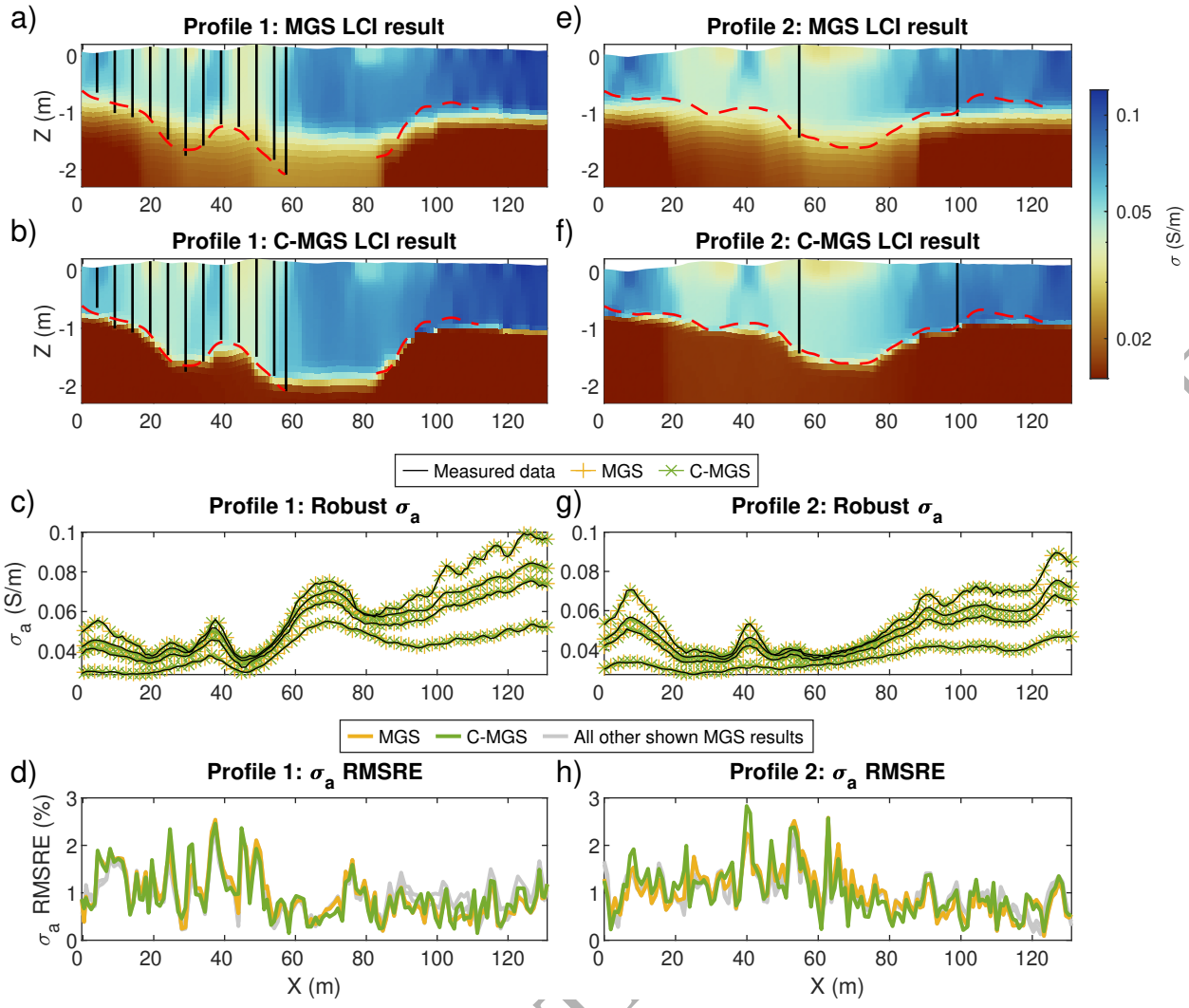


**Figure 6.** Best LCI result (in terms of reconstructing the assumed peat-sand interface) using the MGS approach for (a) Profile 1 and (e) Profile 2 using $\epsilon = 0.01$ and $w = 0.5$. Best LCI result (in terms of reconstructing the assumed peat-sand interface) using the C-MGS approach for (b) Profile 1 and (f) Profile 2 using $\epsilon = 0.01$ and $w = 0.5$. Converted robust $\sigma_a$ data of the measured data (black line) and the modeled data from the MGS (yellow) and C-MGS (green) inversion result for (c) Profile 1 and (g) Profile 2. $\sigma_a$ RMSRE misfit for the MGS (yellow) and the C-MGS (green) inversion result for (d) Profile 1 together with all other MGS inversion results shown in Figs. 4a-c and for (h) Profile 2 together with all other MGS inversion results shown in Figs. 4d-f. In (a), (b), (e) and (f), the black vertical lines indicate the peat thickness as derived from push sounding data, and the red dashed lines indicate the peat-sand interface as interpreted from GPR and push sounding data.

## 5 CONCLUSION

In this work, we present a structurally-constrained inversion approach for FD-EMI data using a regularization approach based on the MGS method. Structural constraints are commonly incorporated into EM data inversion by lowering the smoothness constraint for areas where interfaces are expected to

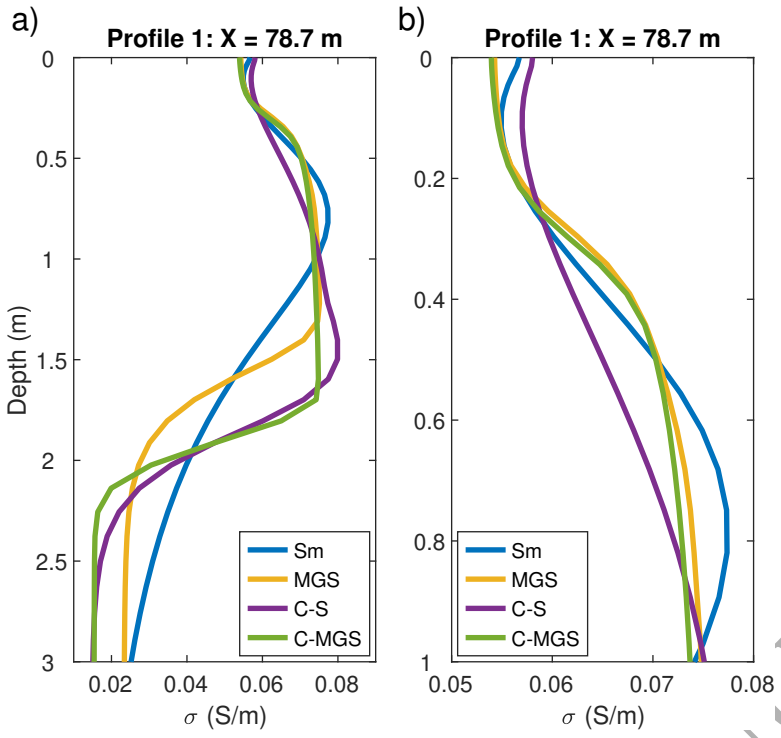


**Figure 7.** (a) LCI results of Profile 1 of the field data example at X = 78.8 m when using the Sm approach (blue), the MGS approach (yellow), the C-S approach (purple), and the C-MGS approach (green). (b) Zoom-in of (a) in order to highlight the differences in the shallow part of the model.

be; so, in this way, the importance of the smoothing regularization term is reduced anytime structural sharp information is available, preventing the smearing of sharp boundaries typical of smooth stabilizers. Clearly, if structural information is available, it must be coherently used in the inversion, but, still, it would be important to incorporate the correct prior information into the inversion for the areas where structural information is not present. The MGS framework discussed here allows for avoiding over-smoothing and retrieval of blocky structures also far from the locations where structural information is provided (in our specific case, via interpretation of GPR data). By means of a 1D synthetic data example we demonstrate that the presented regularization approach retains the basic features of the MGS regularization; i.e., the proposed inversion approach is able to promote sharp results even in areas where no structural assumptions are set. We further extended our analysis to a 2D synthetic case and demonstrated how incorporating structural information is beneficial not only to the retrieval of the exact location of the interfaces but also of the true resistivity values of the different formations.

Finally, we verify the proposed approach on a field survey with the main goal of deriving a reliable estimate of thickness of the studied peat deposits along two selected profiles. In the field example, the structural information used in the C-MGS and C-S schemes is derived from the interpretations of the GPR sections and confirmed by the push soundings. Clearly, the applicability of the proposed

scheme is not limited to the GPR and the push sounding data. The way the structural information is provided to the stabilizers (via the $\boldsymbol{g}$-terms) makes the approach extremely flexible. When comparing the structurally-constrained with the more standard MGS and Sm counterparts, we clearly see that the incorporated structural constraints guide the FD-EMI data inversion towards reconstructions in much better agreement with our expectation (without diminishing the compatibility with the observations). In the investigated field example, a shallower anomaly did not offer a sufficient contrast and continuity to be confidently extracted from the GPR sections, and, consistently it was not possible to use it as structural information. Nevertheless, the proposed C-MGS inversion could retrieve the sharp boundary of that shallow anomaly, whereas the C-S provided smeared results of that shallow feature. Hence, in short, the C-MGS inherits all the advantages of the tunable sparsity stabilizer MGS with the additional possibility to enforce complex structural constraints to the final models.

## 6 ACKNOWLEDGMENTS

This project has been funded by the Deutsche Forschungsgemeinschaft (DFG) (grant number 418056756). We thank Marko Dubnitzki for helping us to collect the field data sets near Kremmen, Germany.

## 7 DATA AVAILABILITY

Data available on request.

## REFERENCES

Ajo-Franklin, J. B., Minsley, B. J., & Daley, T. M., 2007. Applying compactness constraints to differential traveltime tomography, *Geophysics*, **72**(4), R67–R75.

Akca, İ. & Gölebatmaz, Ş. M., 2021. Three-dimensional inversion of DCR data incorporating structural similarity constraint, *Journal of Applied Geophysics*, **184**, 104237.

Altdorff, D., Bechtold, M., Van der Kruk, J., Vereecken, H., & Huisman, J., 2016. Mapping peat layer properties with multi-coil offset electromagnetic induction and laser scanning elevation data, *Geoderma*, **261**, 178–189.

Aster, R. C., Borchers, B., & Thurber, C. H., 2005. *Parameter estimation and inverse problems*, Elsevier.

Bergmann, P., Ivandic, M., Norden, B., Rücker, C., Kiessling, D., Lüth, S., Schmidt-Hattenberger, C., & Juhlin, C., 2014. Combination of seismic reflection and constrained resistivity inversion with an application to 4D imaging of the CO2 storage site, Ketzin, Germany, *Geophysics*, **79**(2), B37–B50.

Beucher, A., Koganti, T., Iversen, B. V., & Greve, M. H., 2020. Mapping of peat thickness using a multi-receiver electromagnetic induction instrument, *Remote Sensing*, **12**(15), 2458.

Blaschek, R., Hördt, A., & Kemna, A., 2008. A new sensitivity-controlled focusing regularization scheme for the inversion of induced polarization data based on the minimum gradient support, *Geophysics*, **73**(2), F45–F54.

Böniger, U. & Tronicke, J., 2010. On the potential of kinematic GPR surveying using a self-tracking total station: Evaluating system crosstalk and latency, *IEEE Transactions on Geoscience and Remote Sensing*, **48**(10), 3792–3798.

Brogi, C., Huisman, J., Pätzold, S., Von Hebel, C., Weihermüller, L., Kaufmann, M., van der Kruk, J., & Vereecken, H., 2019. Large-scale soil mapping using multi-configuration EMI and supervised image classification, *Geoderma*, **335**, 133–148.

Brown, V., Key, K., & Singh, S., 2012. Seismically regularized controlled-source electromagnetic inversion, *Geophysics*, **77**(1), E57–E65.

Cagnoli, B. & Ulrych, T., 2001. Singular value decomposition and wavy reflections in ground-penetrating radar images of base surge deposits, *Journal of applied geophysics*, **48**(3), 175–182.

Clément, R., Pärn, J., Maddison, M., Henine, H., Chaumont, C., Tournebize, J., Uri, V., Espenberg, M., Günther, T., & Mander, Ü., 2020. Frequency-domain electromagnetic induction for upscaling greenhouse gas fluxes in two hemiboreal drained peatland forests, *Journal of Applied Geophysics*, **173**, 103944.

Constable, S. & Weiss, C. J., 2006. Mapping thin resistors and hydrocarbons with marine EM methods: Insights from 1D modeling, *Geophysics*, **71**(2), G43–G51.

Constable, S. C., Parker, R. L., & Constable, C. G., 1987. Occam's inversion: A practical algorithm for generating smooth models from electromagnetic sounding data, *Geophysics*, **52**(3), 289–300.

Couchman, M. J. & Everett, M. E., 2022. Feasibility of a Surface-Based Controlled Source Electromagnetic Method for Detection of Buried Pipelines and Corrosion Effects, *Journal of Infrastructure Systems*, **28**(2), 04022010.

De Smedt, P., Van Meirvenne, M., Saey, T., Baldwin, E., Gaffney, C., & Gaffney, V., 2014. Unveiling the prehistoric landscape at Stonehenge through multi-receiver EMI, *Journal of Archaeological Science*, **50**, 16–23.

Deidda, G. P., Díaz de Alba, P., Rodriguez, G., & Vignoli, G., 2020. Inversion of multiconfiguration complex EMI data with minimum gradient support regularization: a case study, *Mathematical Geosciences*, **52**(7), 945–970.

Doetsch, J., Linde, N., Pessognelli, M., Green, A. G., & Günther, T., 2012. Constraining 3-D electrical resistance tomography with GPR reflection data for improved aquifer characterization, *Journal of Applied Geophysics*, **78**, 68–76.

Favetto, A., Pomposiello, C., Booker, J., & Rossello, E. A., 2007. Magnetotelluric inversion constrained by seismic data in the Tucumán Basin (Andean Foothills, 27 S, NW Argentina), *Journal of Geophysical Research: Solid Earth*, **112**(B9).

Feng, Y., Zhang, J., & Wang, S., 2017. A new edge detection algorithm based on canny idea, in *AIP Conference Proceedings*, vol. 1890, p. 040011, AIP Publishing LLC.

Fiandaca, G., Doetsch, J., Vignoli, G., & Auken, E., 2015. Generalized focusing of time-lapse changes with applications to direct current and time-domain induced polarization inversions, *Geophysical Journal International*, **203**(2), 1101–1112.

Guillemoteau, J. & Tronicke, J., 2015. Non-standard electromagnetic induction sensor configurations: Evaluating sensitivities and applicability, *Journal of Applied Geophysics*, **118**, 15–23.

Guillemoteau, J., Simon, F. X., Lück, E., & Tronicke, J., 2016. 1D sequential inversion of portable multi-configuration electromagnetic induction data, *Near Surface Geophysics*, **14**, 411–420.

Guillemoteau, J., Christensen, N. B., Jacobsen, B. H., & Tronicke, J., 2017. Fast 3D multichannel deconvolution of electromagnetic induction loop-loop apparent conductivity data sets acquired at low induction numbers, *Geophysics*, **82**(6), E357–E369.

Guillemoteau, J., Simon, F.-X., Hulin, G., Dousteyssier, B., Dacko, M., & Tronicke, J., 2019. 3-D imaging of subsurface magnetic permeability/susceptibility with portable frequency domain electromagnetic sensors for near surface exploration, *Geophysical Journal International*, **219**(3), 1773–1785.

Guillemoteau, J., Vignoli, G., Barreto, J., & Sauvin, G., 2022. Sparse laterally constrained inversion of surface wave dispersion curves via minimum gradient support regularization, *Geophysics*, **87**(3), 1–38.

Haber, E., 2014. *Computational methods in geophysical electromagnetics*, SIAM.

Jadoon, K. Z., Moghadas, D., Jadoon, A., Missimer, T. M., Al-Mashharawi, S. K., & McCabe, M. F., 2015. Estimation of soil salinity in a drip irrigation system by using joint inversion of multicoil electromagnetic induction measurements, *Water Resources Research*, **51**, 3490–3504.

Jiang, C., Igel, J., Dlugosch, R., Müller-Petke, M., Günther, T., Helms, J., Lang, J., & Winsemann, J., 2020. Magnetic resonance tomography constrained by ground-penetrating radar for improved hydrogeophysical characterization, *Geophysics*, **85**(6), JM13–JM26.

Klose, T., Guillemoteau, J., Vignoli, G., & Tronicke, J., 2022. Laterally constrained inversion (LCI) of multi-configuration EMI data with tunable sharpness, *Journal of Applied Geophysics*, **196**, 104519.

Kristiansen, S. M., Stott, D., Christiansen, A. V., Henriksen, P. S., Jessen, C., Mortensen, M. F., Pedersen, J. B., Sindbæk, S. M., & Ulriksen, J., 2022. Non-destructive 3D prospection at the Viking Age fortress Borgring, Denmark, *Journal of Archaeological Science: Reports*, **42**, 103351.

Last, B. & Kubik, K., 1983. Compact gravity inversion, *Geophysics*, **48**(6), 713–721.

Martini, E., Werban, U., Zacharias, S., Pohle, M., Dietrich, P., & Wollschläger, U., 2017. Repeated electromagnetic induction measurements for mapping soil moisture at the field scale: Validation with data from a wireless soil moisture monitoring network, *Hydrology and Earth System Sciences*, **21**(1), 495–513.

McLachlan, P., Blanchy, G., Chambers, J. E., Sorensen, J., Uhlemann, S., Wilkinson, P. B., & Binley, A., 2020. Electromagnetic induction methods reveal wetland hydrogeological structure and properties, *Earth and Space Science Open Archive*.

McNeill, J. D., 1980. Electromagnetic terrain conductivity measurements at low induction numbers, *Technical Note TN-6, Geonics Ltd*.

Paepen, M., Hanssens, D., De Smedt, P., Walraevens, K., & Hermans, T., 2020. Combining resistivity and

frequency domain electromagnetic methods to investigate submarine groundwater discharge in the littoral zone, *Hydrology and Earth System Sciences*, **24**(7), 3539–3555.

Portniaguine, O. & Zhdanov, M. S., 1999. Focusing geophysical inversion images, *Geophysics*, **64**(3), 874–887.

Rudolph, S., Wongleecharoen, C., Lark, R. M., Marchant, B. P., Garré, S., Herbst, M., Vereecken, H., & Weihermüller, L., 2016. Soil apparent conductivity measurements for planning and analysis of agricultural experiments: A case study from Western-Thailand, *Geoderma*, **267**, 220–229.

Thibaut, R., Kremer, T., Royen, A., Ngun, B. K., Nguyen, F., & Hermans, T., 2021. A new workflow to incorporate prior information in minimum gradient support (MGS) inversion of electrical resistivity and induced polarization data, *Journal of Applied Geophysics*, **187**, 104286.

Thiesson, J., Tabbagh, A., Dabas, M., & Chevalier, A., 2018. Characterization of buried cables and pipes using electromagnetic induction loop-loop frequency-domain devicesBuried cable detection using EMI, *Geophysics*, **83**(1), E1–E10.

Uhlemann, S., Chambers, J., Wilkinson, P., Maurer, H., Merritt, A., Meldrum, P., Kuras, O., Gunn, D., Smith, A., & Dijkstra, T., 2017. Four-dimensional imaging of moisture dynamics during landslide reactivation, *Journal of Geophysical Research: Earth Surface*, **122**(1), 398–418.

Vereecken, H., Huisman, J. A., Hendricks Franssen, H. J., Brüggemann, N., Bogena, H. R., Kollet, S., Javaux, M., van der Kruk, J., & Vanderborght, J., 2015. Soil hydrology: Recent methodological advances, challenges, and perspectives, *Water Resources Research*, **51**(4), 2616–2633.

Vignoli, G., Deiana, R., & Cassiani, G., 2012. Focused inversion of vertical radar profile (VRP) traveltime data, *Geophysics*, **77**(1), H9–H18.

Vignoli, G., Fiandaca, G., Christiansen, A. V., Kirkegaard, C., & Auken, E., 2015. Sharp spatially constrained inversion with applications to transient electromagnetic data, *Geophysical Prospecting*, **63**(1), 243–255.

Vignoli, G., Guillemoteau, J., Barreto, J., & Rossi, M., 2021. Reconstruction, with tunable sparsity levels, of shear wave velocity profiles from surface wave data, *Geophysical Journal International*, **225**(3), 1935–1951.

von Hebel, C., Rudolph, S., Mester, A., Huisman, J., Kumbhar, P., Vereecken, H., & van der Kruk, J., 2014. Three-dimensional imaging of subsurface structural patterns using quantitative large-scale multiconfiguration electromagnetic induction data, *Water Resources Research*, **50**, 2732–2748.

von Hebel, C., Reynaert, S., Pauly, K., Janssens, P., Piccard, I., Vanderborght, J., van der Kruk, J., Vereecken, H., & Garré, S., 2021. Toward high-resolution agronomic soil information and management zones delineated by ground-based electromagnetic induction and aerial drone data, *Vadose Zone Journal*, **20**(4), e20099.

Wagner, F. M. & Uhlemann, S., 2021. An overview of multimethod imaging approaches in environmental geophysics, *Advances in Geophysics*, **62**, 1–72.

Wait, J., 1982. *Geo-electromagnetism*, Academic Press Inc.

Ward, S. H. & Hohmann, G. W., 1988. Electromagnetic theory for geophysical applications, in *Electromagnetic Methods in Applied Geophysics*, pp. 131–312, Society of Exploration Geophysicists.

Yan, P., Kalscheuer, T., Hedin, P., & Garcia Juanatey, M. A., 2017. Two-dimensional magnetotelluric inver-

sion using reflection seismic data as constraints and application in the COSC project, *Geophysical Research Letters*, **44**(8), 3554–3563.

Zhdanov, M., Vignoli, G., & Ueda, T., 2006. Sharp boundary inversion in crosswell travel-time tomography, *Journal of Geophysics and Engineering*, **3**(2), 122–134.

Zhdanov, M. S., 2002. *Geophysical inverse theory and regularization problems*, Elsevier.